Special Collection

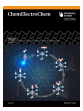

# The Dual Effect of Coordinating –NH Groups and Light in the Electrochemical $CO_2$ Reduction with Pyridylamino Co Complexes

Sergio Fernández,[a, b] Santiago Cañellas,[a] Federico Franco,[a] Josep M. Luis,[c] Miquel À. Pericàs,*[a, d] and Julio Lloret-Fillol*[a, e]

*Dedicated to JM Savéant for his pioneering work on molecular electrochemistry.*

$CO_2$ electroreduction could be improved by applying conceptualized strategies to overcome catalytic bottlenecks. In this regard, we report two new cobalt(II) complexes [Co($Py_2^RN_3$)(OTf)](OTf) (**Co$^R$**, R=H, Me) based on a new $C_2$-symmetric pentacoordinate chiral ligand that are active on the electrochemical $CO_2$ reduction to CO. One of the complexes has a N–H group oriented towards the $CO_2$ binding site (**Co$^H$**), while the other has a N–Me group with the same orientation (**Co$^{Me}$**), as showed by X-ray diffraction. We have studied the effect of introducing hydrogen bonding sites, *i.e.* N–H in **Co$^H$**, as a strategy to stabilize reaction intermediates. The complex bearing coordinating unprotected N–H group (**Co$^H$**) displays catalytic $CO_2$ reduction at the $Co^{II/I}$ redox potential (−1.9 V vs. Fc, ca. 40 % $FY_{CO}$) whereas **Co$^{Me}$** shows $CO_2$ reduction at the $Co^{I/0}$ redox pair. FTIR-SEC and DFT calculations identified a $[Co^I–CO]^+$ cation as catalytic intermediate. The beneficial effect of the N–H group has been attributed to the stabilization of reaction intermediates or transition states and by the larger electron-donating capacity, thus enhancing the nucleophilic character of the $Co^I$ intermediate. The study also points to the CO dissociation from the Co(I)–CO resting state intermediate as one of the bottlenecks of the catalytic cycle, which can be overcome with light irradiation, resulting in an increase of the total CO production (−1.9 V, 81 % $FY_{CO}$, 11.2 $TON_{CO}$) at the $Co^{II/I}$ redox potential.

## 1. Introduction

The current environmental situation, along with the increasing energy demand of our society, has led to rising interest in developing new and more effective methods to store the energy obtained from renewable sources.[1] One of the most promising approaches is transforming solar energy into chemical energy through an electrical potential. Despite its inherent thermodynamic stability, $CO_2$ has become a target molecule to activate due to its high availability as a by-product from the oxidation of organic matter and its versatility as a potential $C_1$ building block in the synthesis of fuels and fine chemicals.[2] In particular, the efficient multielectron reduction of $CO_2$ is still a challenge in both homogeneous and heterogeneous catalysis.[3] Whereas heterogeneous systems are foreseen as the most suitable ones for large-scale $CO_2$ reduction, the control over the product selectivity of the process is still very challenging.[4] In contrast, homogeneous complexes are generally less stable than materials and, except for a few examples, they are limited to the formation of two-electron reduction products *i.e.* CO and formic acid.[5] Nonetheless, most mechanistic studies reported so far refer to homogeneous systems.[6] Moreover, recent reports show promising results in terms of durability and catalytic performance of molecular entities anchored over conductive surfaces or by incorporating catalytically active units in well-defined reticular frameworks (MOFs, COFs) and coordination polymers.[7]

Fundamental studies together with spectroscopy, electrochemistry, and computational modelling have allowed to interrogate the elemental steps, and to identify the thermodynamic and kinetic factors governing the $CO_2$-to-CO reduction catalytic cycle.[8] As it is shown in Scheme 1, the first main chemical step in the $CO_2$ reduction mechanism is the formation of a metal-carboxylate adduct $[M–CO_2]^{n-1}$ after the $CO_2$ binding to a low-

[a] S. Fernández, Dr. S. Cañellas, Dr. F. Franco, Prof. Dr. M. À. Pericàs, Prof. Dr. J. Lloret-Fillol
Institute of Chemical Research of Catalonia (ICIQ)
The Barcelona Institute of Science and Technology (BIST)
Av. Països Catalans 16, 43007 Tarragona, Spain
E-mail: mapericas@iciq.es
jlloret@iciq.es
[b] S. Fernández
Department de Química Física i Inorgànica
Universitat Rovira i Virgili
43007 Tarragona, Spain
[c] Dr. J. M. Luis
Institut de Química Computacional i Catàlisi (IQCC) and Departament de Química
Universitat de Girona
Campus Montilivi
17003 Girona, Spain
[d] Prof. Dr. M. À. Pericàs
Departament de Química Inorgànica i Orgànica
Universitat de Barcelona
08080 Barcelona, Spain
[e] Prof. Dr. J. Lloret-Fillol
Catalan Institution for Research and Advanced Studies (ICREA)
Passeig Lluís Companys 23,
08010 Barcelona, Spain

Supporting information for this article is available on the WWW under https://doi.org/10.1002/celc.202100859

Special Collection *An invited contribution to a joint Special Collection in memory of Prof. Jean-Michel Savéant.*

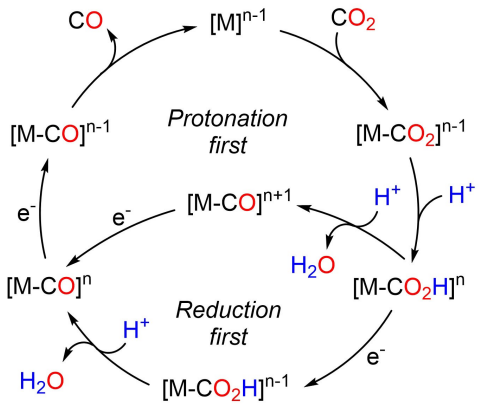


**Scheme 1.** Simplified catalytic cycle for the proton-assisted $CO_2$-to-CO reduction.

valent intermediate $[M]^{n-1}$. Successive protonation and reduction steps trigger the C–O bond cleavage giving a metal-carbonyl intermediate. The C–O bond cleavage has been identified as the rate determining step (rds) of the electrocatalytic $CO_2$-to-CO reduction mechanism mediated by several molecular catalysts.[9] Finally, the catalytically active low-valent species is recovered after the release of CO. In this regard, our group has recently reported that the CO release from $[Co–CO]^+$ in a pyridylamino cobalt complex is highly endergonic.[10] In this case, the $CO_2$ reduction rate depends not only on the $CO_2$ binding and C–O bond cleavage steps but also on the CO release.

Different strategies have been employed to improve the $CO_2$ reduction to CO by including selective interactions with the postulated reaction intermediates. For instance, the beneficial effect of the incorporation of N–H, O–H or S–H groups at the periphery of the ligand suggested that the metal-carboxylate intermediates are stabilized through hydrogen bonding interactions. This is also the case for the classical Ni and Co cyclam-like complexes (Figure 1, i–ii) where $[M–CO_2]^{n-1}$ is postulated as being stabilized by hydrogen bonding interactions with the N–H groups of the ligand.[11a,b] Similarly, the C–O bond cleavage can be boosted by intramolecular protonation with a local proton source as in the case of the Fe-porphyrin modified with internal *o*-phenol groups reported by Savéant and co-workers and other examples based on organometallic Mn, Fe and Co complexes (Figure 1,iii–vii).[9g,11c–f] Besides, the $CO_2$ reduction rate can still be limited by other steps in the reaction mechanism such as the CO release. In this line, different strategies have been employed to modulate the stability of the M–CO intermediates.[12] We also proposed the use of light as an energy input to boost the catalytic cycle by labilising the CO ligand.[10]

Herein, we report the synthesis of two new non-macrocyclic cobalt complexes and their catalytic activity in electroreduction of $CO_2$. The main difference between the two metal complexes is the substitution of the coordinating amine ligands ([Co-($\mathbf{L^R}$)(OTf)](OTf), R=H for $\mathbf{Co^H}$ and R=$CH_3$ for $\mathbf{Co^{Me}}$) which is used to account for the effect of coordinating N–H bonds to the metal center in the electrochemical $CO_2$ reduction to CO. We have rationalized the effect of coordinating N–H groups by using cyclic voltammetry (CV) as well as *in situ* infrared spectroelectrochemistry (FTIR-SEC) under $^{12}CO_2$ and $^{13}CO_2$, controlled potential electrolysis (CPE) and density functional theory calculations (DFT). Finally, we combined two strategies to produce sustained $CO_2$-to-CO catalysis at the $Co^{II/I}$ redox coupled rather that the $Co^{I/0}$, which implies an about 500 mV decrease in overpotential.

## 2. Results and Discussion

### 2.1. Synthesis and Characterization

For the synthesis of the two pyridylamino ligands $\mathbf{L^H}$ and $\mathbf{L^{Me}}$ starting from the $C_2$-symmetric chiral triamine, we have adapted a previously reported methodology for the synthesis of tetracoordinate pyridylamino ligands (Scheme 2).[13] The synthesis of the $C_2$-symmetric chiral triamine was recently reported by Pericàs and co-workers.[14] Cobalt complexes $\mathbf{Co^H}$ and $\mathbf{Co^{Me}}$ were synthesized following the scheme in Figure 2 and fully characterized (section 1 in the SI).

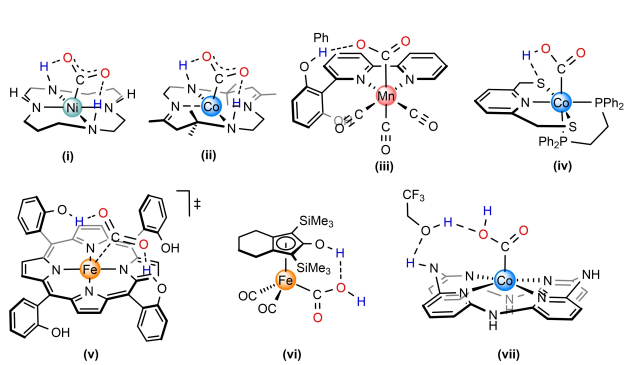


**Figure 1.** Schematic representation of the ligand effect in the $CO_2$ binding (i-ii) and in the protonation events and C–O bond cleavage of the $CO_2$-to-CO reduction mechanism (iii-vi).[9g,11]

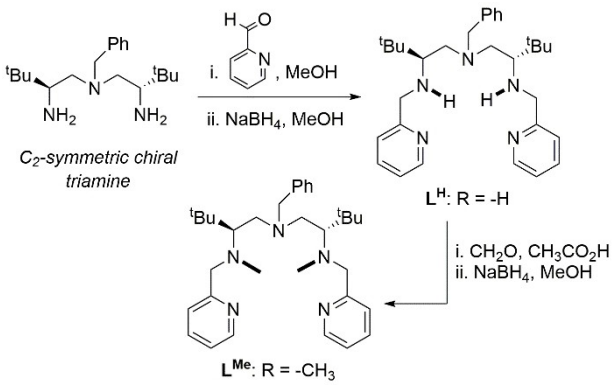


**Scheme 2.** General scheme for the synthesis of ligands $\mathbf{L^H}$ and $\mathbf{L^{Me}}$ starting from a $C_2$-symmetric chiral triamine.

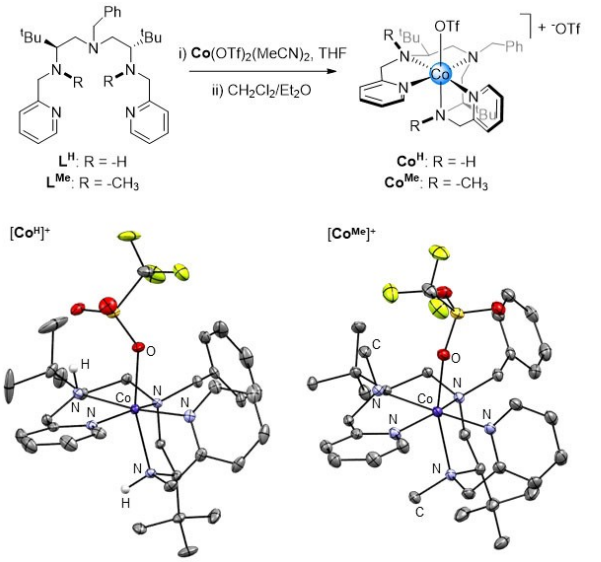


**Figure 2.** General synthetic scheme and ORTEP plot of **Co$^{H}$** (top) and **Co$^{Me}$** (bottom) X-ray structures with ellipsoids at the 50% probability. Non-relevant hydrogen atoms and non-coordinating triflate anions have been omitted for clarity.

The $^{1}$H-NMR spectra of the two complexes showed strong paramagnetic character, with broad signals in the spectral window between −100 and 300 ppm, which is prototypical for a high-spin Co$^{II}$ ($d^7$) complex.[15] High resolution electro-spray ionization mass spectrometry (HR-ESI-MS) of **Co$^{H}$** and **Co$^{Me}$** in acetonitrile solution revealed the monocharged [M-(OTf)]$^{+}$ ions at m/z 695.2531 and 723.2844, respectively (Figures S1 and S2). X-ray diffraction data of monocrystals of **Co$^{H}$** and **Co$^{Me}$** confirmed the formation of distorted octahedral complexes formed by a pentadentate ligand coordinated to the Co center by the three N atoms of the chiral backbone (d(Co–N) ca. 2.13–2.33 Å), the two pyridynes (d(Co–N) ca. 2.10–2.16 Å) and a triflate anion (d(Co–O) ca. 2.16 Å). These bond distances are typical of Co$^{II}$ aminopyridyne coordination complexes.[16] Relevant bond lengths are summarized in Figures S3 and S4.

Interestingly, the X-ray diffraction structure of **Co$^{H}$** (Figure 2) shows one of the two N–H groups in the complex pointing towards the coordinating position occupied by the mono-coordinating triflate ($^{-}$OTf) anion. However, the solution $^{1}$H-NMR in of the **Co$^{H}$** complex suggested the presence a major isomer (91%) and a minor one (9%) (see section 2.1 of the SI). Our DFT calculations qualitatively agree with this distribution, since the isomer observed by X-ray diffraction and the most stable one predicted by the calculations are the same ($\Delta G =$ 4.2 kcal·mol$^{-1}$, Figure S5). For **Co$^{Me}$**, a single isomer was observed in solution and in the X-ray diffraction structure, with the ligand in the same conformation found for the major isomer for **Co$^{H}$**. Since both **Co$^{H}$** and **Co$^{Me}$** complexes have the same conformational structure, we proposed that a direct comparison of the electrocatalytic $CO_2$ reduction of both systems could lead to insights on the effect of the N–H group *versus* the N–Me one on the reduction process.

### 2.2. Electrochemistry in Dry MeCN

CV of complexes **Co$^{H}$** and **Co$^{Me}$** in anhydrous acetonitrile under Ar atmosphere showed reversible Co$^{II/I}$ waves at $E_{1/2}$ of −1.86 and −1.66 V, respectively (Figure 3, Eq. 1). The Co$^{II/I}$ redox couple of the two complexes diffused according to the Randles-Ševčík equation (Figures S6 and S7). The 200 mV shift to more negative reduction potential of the **Co$^{H}$** complex relative to **Co$^{Me}$** is consistent with a more electron-rich Co$^{II}$ centre, due to the stronger donor coordinating capacity of the N–H groups. An analogous anodic shift of the M$^{II/I}$ redox potential was found for the methylated Ni cyclam derivative compared with the non-methylated complex.[17]

$$[Co^{II}]^{2+} + e^{-} \rightleftharpoons [Co^{I}]^{+} \quad (1)$$

$$[Co^{I}]^{+} + CO_2 \xrightarrow{k_{obs}} [Co^{III} - CO_2]^{+} \quad (2)$$

Upon bubbling $CO_2$ through the solution of **Co$^{H}$**, the first one-electron reduction becomes irreversible and the peak potential ($E_p$) anodically shifts to −1.80 V (Figure 4). This behaviour has been reported for other pyridylamino and macrocyclic Co complexes and indicates a strong interaction between the electrochemically generated Co$^{I}$ species and the $CO_2$ molecule substrate to form a metal-carboxylate complex through an electrochemical (EC) mechanism (Eq. 2).[8] Under *pure kinetic conditions, i.e.* steady state conditions in close proximity to the electrode surface, the magnitude of such interaction can be estimated by using Eq. 3 which correlates the potential shift of the Co$^{II/I}$ redox potential observed under $CO_2$ with the kinetic constant for $CO_2$ binding ($k_{obs}$), the scan rate (ν) and the concentration of $CO_2$ in solution (under saturation conditions in MeCN, $[CO_2] = 0.28$ M).[18]

$$E_p = E_{1/2}(Co^{II/I}) - 0.78\frac{RT}{F} + \frac{RT}{2F} ln \frac{RTk_{obs}[CO_2]}{Fv} \quad (3)$$

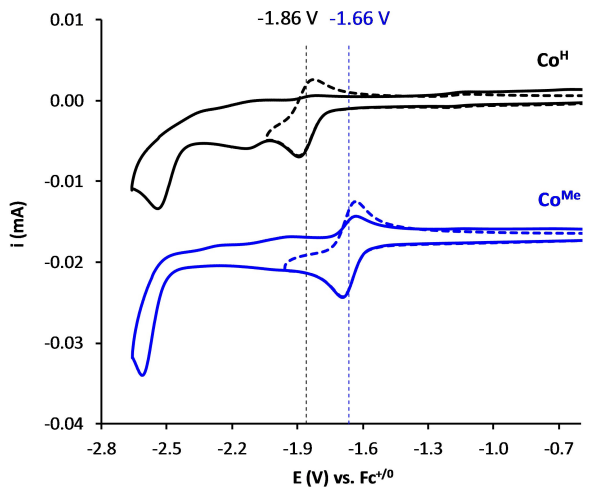


**Figure 3.** Cyclic voltammograms (0.1 V·s$^{-1}$) of complexes **Co$^{H}$** (top) and **Co$^{Me}$** (bottom) at 0.4 mM in TBAPF$_6$/MeCN 0.1 M under Ar atmosphere.

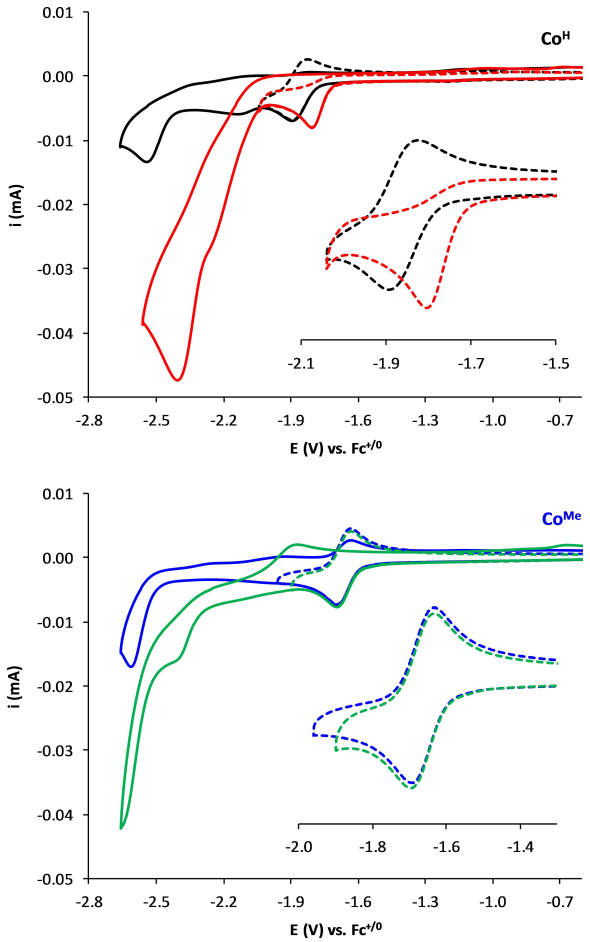


**Figure 4.** Cyclic voltammograms (0.1 $V \cdot s^{-1}$) of complexes **Co$^{H}$** (a) and **Co$^{Me}$** (b) at 0.4 mM in $TBAPF_6$/MeCN 0.1 M under Ar (black) and $CO_2$ atmosphere (red). The insets show a magnification of the $Co^{II/I}$ process in each case.

For **Co$^{H}$**, a $k_{obs} = 7 \cdot 10^3\ M^{-1} \cdot s^{-1}$ was obtained (60 mV shift at 0.1 $V \cdot s^{-1}$) which is in the same order of magnitude than other reported $k_{CO2}$ involving $Co^{I}$ species.[10] Contrarywise, the $Co^{II/I}$ event of the methylated counterpart (**Co$^{Me}$**) remains unchanged under $CO_2$-saturated conditions, without any observable shift of the peak potential, nor reversibility loss in the CV timescale (0.1 $V \cdot s^{-1}$). Thus, in the absence of an added Brønsted acid, the reaction of $Co^{I}$ with the substrate is faster for **Co$^{H}$** than for **Co$^{Me}$**. DFT calculations showed that the binding of $CO_2$ to $Co^{I}$ ($\Delta G_{CO2}$) is exergonic by −0.6 kcal·mol$^{-1}$ for **Co$^{H}$** and endergonic by 6.4 kcal·mol$^{-1}$ for **Co$^{Me}$**. This effect can be explained by the stronger nucleophilic character of the $Co^{I}$ intermediate of **Co$^{H}$**. On the other hand, the presence of polar N–H groups coordinated to the metal centre can either stabilize the transition state (TS), the reaction product *i.e.* $[Co–CO_2]^+$, or both of them through direct intramolecular hydrogen bonding. We cannot fully rule out a certain steric contribution of the methyl group in the behavior of **Co$^{Me}$**.

The increase of the current observed at more negative potentials in the CVs for both **Co$^{H}$** and **Co$^{Me}$** suggested that both catalysts could be active for the catalytic $CO_2$ reduction. However, **Co$^{H}$** displays a 4-fold current increase compared to the one-electron process under Ar, whereas **Co$^{Me}$** shows a 2.3-fold current increase at −2.45 V. These results suggest that **Co$^{H}$** could provide a higher catalytic activity than **Co$^{Me}$** at lower overpotentials which agrees with a positive effect of the coordinating N–H groups assisting the C–O bond cleavage step.

### 2.3. Spectroelectrochemistry under $CO_2$

To investigate the nature of the potential reactivity of cobalt species towards $CO_2$ at mild (over)potentials, we performed *in-situ* FTIR-SEC recorded upon reduction at the $Co^{II/I}$ redox wave of **Co$^{H}$** and **Co$^{Me}$** under $CO_2$-saturated conditions (Figure 5). In both cases we observed an evolution of the FTIR spectrum when maintaining the applied redox potential at the first reduction event. While in the case of **Co$^{H}$**, a band at 1896 $cm^{-1}$ grows upon reduction, for complex **Co$^{Me}$** the raising feature is observed at 1910 $cm^{-1}$. The frequency of these vibrations lies in the $Co^{I}$–CO stretching region.[19] Labelling studies under $^{13}CO_2$ atmosphere show the appearance of the corresponding $^{13}C$-labelled intermediate at 1852 $cm^{-1}$ and 1866 $cm^{-1}$, for **Co$^{H}$** and **Co$^{Me}$**, respectively. The observed $^{12}C$-$^{13}C$ isotopic shift of 44 $cm^{-1}$ is consistent with the formation of a $[Co^{I}–CO]^+$ intermediate.

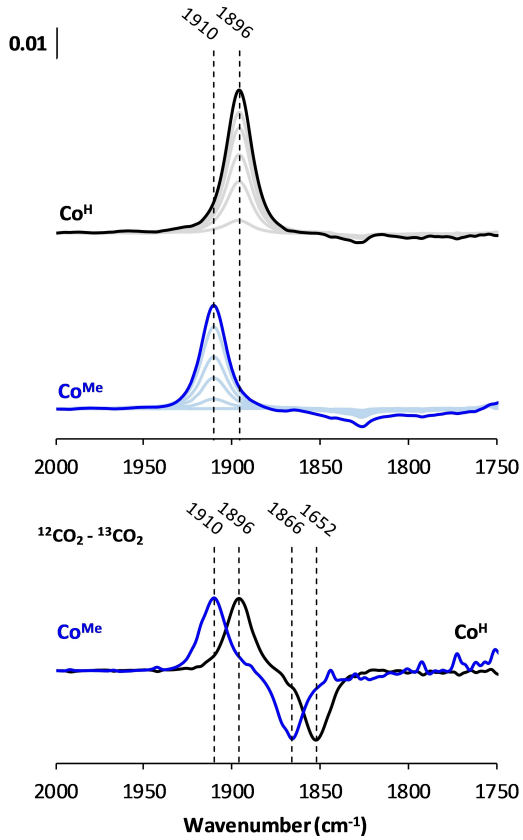


**Figure 5.** Thin layer *in situ* FTIR-SEC under $CO_2$ of **Co$^{H}$** (black) and **Co$^{Me}$** (blue). The formation of metal carbonyls starts at the $Co^{II/I}$ wave. [Co] = 6 mM in $TBAPF_6$/MeCN 0.2 M. Top) Differential spectra (Abs-Abs$_0$) *vs.* wavenumber. Bottom) Difference between the normalized spectra obtained under $^{12}CO_2$ and $^{13}CO_2$.

We note that the CV of **Co$^{Me}$** under $CO_2$ does not evidence the formation of a Co–CO species. Nonetheless, the FTIR-SEC experiment, which takes place after several minutes, allows for the observation of a slow chemical processes leading to the formation the $[Co^{I}–CO]^{+}$ ion. This delay between CV and FTIR-SEC, indicates that the reaction between the one-electron reduced **Co$^{Me}$** intermediate is much slower than the time scale of our CV experiments (100 $mV \cdot s^{-1}$).

We recently demonstrated that the formation of $[Co^{I}–CO]^{+}$ at the $Co^{II/I}$ redox potential of a tetracoordinate pyridylamino cobalt complex can occur through two different mechanistic pathways depending on the reaction conditions.[10] In aprotic media, the C–O bond cleavage step can be assisted by a second $CO_2$ molecule through the so-called $CO_2$ reductive disproportionation mechanism (Eq. 4).

$$[Co^{III} - CO_2]^{+} + e^{-} + CO_2 \rightarrow [Co^{II} - CO]^{2+} + CO_3^{2-} \quad (4)$$

In the presence of an added or adventitious proton source, the same step can be promoted by the double protonation Co-carboxylate adduct (Eq. 5). Both pathways result in the formation of $HCO_3^{-}/CO_3^{2-}$ (Eq. 6) together with $[Co^{II}–CO]^{2+}$. Finally, at the $Co^{II/I}$ redox potential, the latter intermediate is reduced to $[Co^{I}–CO]^{+}$ (Eq. 7) since $E_{Co(II/I)–CO}$ is less negative than $E_{Co(II/I)}$.

$$[Co^{III} - CO_2]^{+} + e^{-} + H_2O \rightarrow [Co^{II} - CO]^{2+} + 2OH^{-} \quad (5)$$

$$OH^{-} + CO_2 \rightarrow HCO_3^{-} \quad (6)$$

$$[Co^{II} - CO]^{2+} + e^{-} \rightarrow [Co^{I} - CO]^{+} \quad (7)$$

The red shift of 14 $cm^{-1}$ observed in the CO stretching frequencies of **Co$^{H}$** in comparison to **Co$^{Me}$** suggested that the interaction of $Co^{I}$ with the CO ligand in the Co–CO intermediate of **Co$^{H}$** is stronger than in **Co$^{Me}$**. Indeed, the DFT calculated IR spectra for the two $[Co^{I}–CO]^{+}$ complexes present an excellent match of our experimental results with theoretical values for the CO stretching bands of 1892 and 1910 $cm^{-1}$ for **Co$^{H}$** and **Co$^{Me}$**, respectively (Figure 6). This agrees with a stronger π-backbonding from the metal to the CO ligand induced by the highly basic coordinating N–H groups.

Other remarkable spectral differences in the region of C=O stretching bands of both complexes also exist (Figure 7). In the case of **Co$^{H}$**, the typical bands of free $HCO_3^{-}$ (1684 $cm^{-1}$) and $CO_3^{2-}$ (1646 $cm^{-1}$) increase along with the one of $[Co^{I}–CO]^{+}$, suggesting the catalytic formation of CO and $HCO_3^{-}/CO_3^{2-}$ according to Eq. 4–6.[20] Before the formation of free $HCO_3^{-}/CO_3^{-2}$, a transient broad signal appears at 1670 $cm^{-1}$ which can be tentatively assigned to a $[Co^{II}–CO_3]$ type of intermediate. The same signal shifts to 1630 $cm^{-1}$ under $^{13}CO_2$ (Figures S12 top). At more negative potentials, both complexes show a transient $Co^{0}$–CO intermediate at 1818 $cm^{-1}$ which evolves to a new carbonyl species with $\nu_{st}(CO) = 1893\ cm^{-1}$ that has been assigned to $[Co(CO)_4]^{-}$ (Figures S14 and S15).[21] The formation of $[M(CO)_x]^{y}$ species under catalytic IR-SEC conditions is well-known for other first-row transition metal complexes.[12a,22]

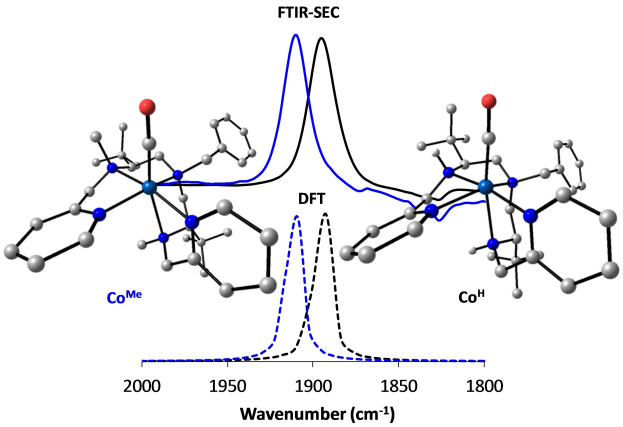


**Figure 6.** Comparison between the normalized FTIR (solid lines) and DFT (dashed lines) IR spectra (vertical axis in arbitrary units) of the $[Co^{I}–CO]^{+}$ intermediate of complexes **Co$^{H}$** (black) and **Co$^{Me}$** (blue). DFT minimized geometries of the latter intermediates.

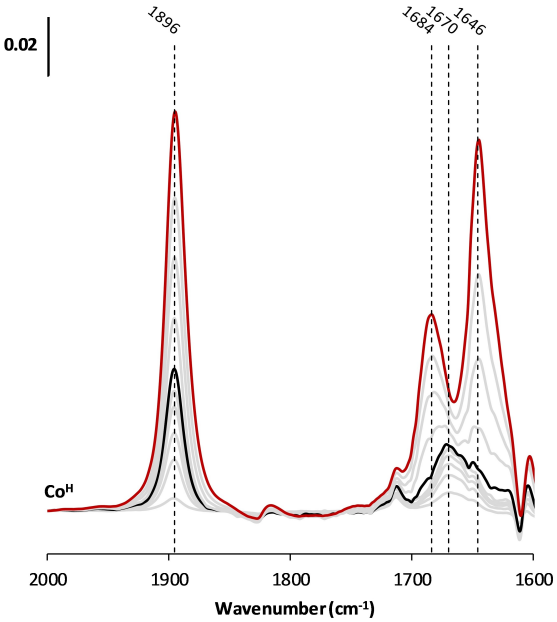


**Figure 7.** Thin layer *in situ* FTIR-SEC under $CO_2$ of **Co$^{H}$** at ca. −1.4 V vs. Ag wire (black) and at −1.6 V vs. Ag wire (red). [Co] = 6 mM in $TBAPF_6$/MeCN 0.2 M. Differential spectra ($Abs–Abs_0$) *vs.* wavenumber.

## 2.4. Electrochemistry in the Presence of Water

CV experiments of **Co$^{H}$** under $CO_2$ with increasing amounts of $H_2O$ revealed a gradual current increase at the $Co^{II/I}$ redox process, reaching a maximum 3-fold increase at 10% added $H_2O$ (Figures 8 and S8a). Based on this experiment, we hypothesized that the observed current increment is due to the formation of $[Co^{I}–CO]^{+}$ at the $E_{Co(II/I)}$ of **Co$^{H}$** which consumes three electrons starting from $Co^{II}$ (Eq. 1–6).

Contrarywise, the CV of **Co$^{Me}$** in the presence of water does not show a remarkable current increase at the $Co^{II/I}$ wave and keeps quasi-reversible suggesting a much slower $CO_2$ binding,

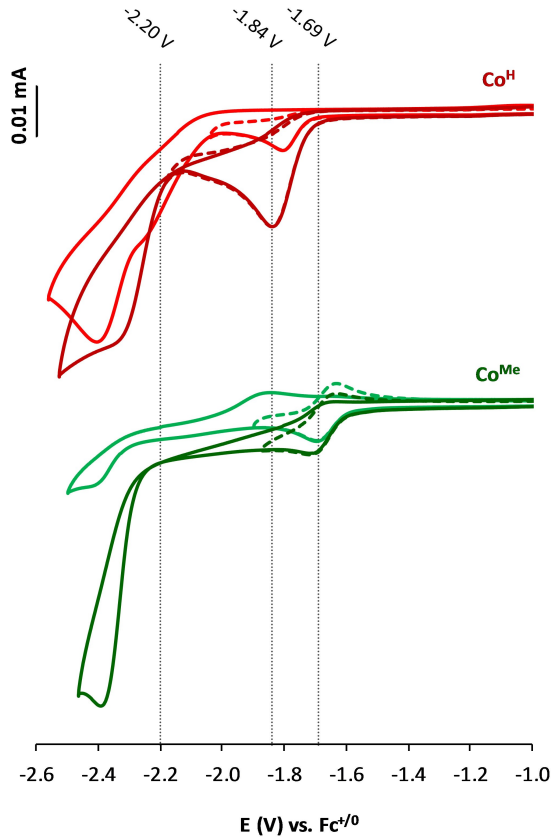


**Figure 8.** CVs of $Co^{H}$ and $Co^{Me}$ under $CO_2$ in anhydrous electrolyte (red and green, respectively) and with a 10% of added $H_2O$ (dark red and dark green, respectively). [Co] = 0.4 mM at 0.1 $V \cdot s^{-1}$ over a GC working electrode (Ø = 0.3 cm) in MeCN/$TBAPF_6$.

even in a protic environment (Figure S9a). A similar behavior was also described for Ni-cyclam catalysts in wet MeCN and the current increase observed for the unsubstituted Ni-cyclam catalyst was attributed to an apparent catalytic process.[17] The apparent catalytic behaviour at the $Co^{II/I}$ wave of $Co^{H}$ is consistent with the formation of $HCO_3^-/CO_3^{2-}$ observed by FTIR-SEC.

Both $Co^{H}$ and $Co^{Me}$ show a comparable current increase in the CV at more negative potentials ($E_{app} < -2.2$ V). As we have previously reported, the catalytic $CO_2$ reduction to CO involves the formation of a $Co^0$–CO species. However, both $Co^{H}$ and $Co^{Me}$ present a non-negligible catalytic response towards $H_2$ production as observed in the CVs at increasing amounts of $H_2O$ (up to 10%) under Ar (Figures S8b and S9b).

Controlled potential electrolysis (CPE) experiments in wet electrolyte (1–10% (v/v) of $H_2O$) produced CO as the major $CO_2$ reduction product (Table 1). CPE of $Co^{H}$ with a 1% (v/v) of added $H_2O$ at −2.2 V vs. $Fc^{+/0}$ generated 0.5 $TON_{CO}$ after 3 h, whereas $Co^{Me}$ produced only 0.2 $TON_{CO}$ under the same conditions. In terms of current efficiency, $Co^{H}$ and $Co^{Me}$ provide 19% and 9% $FY_{CO}$ after 60 min of CPE, respectively. In the case of $Co^{Me}$, $H_2$ was also detected in the headspace after CPE and no $CO_2$ reduction products were identified in solution by $^1$H-NMR for both $Co^{H}$ and $Co^{Me}$. These results are in line with the low $FY_{CO}$ obtained with other pyridylamino Co complexes and

**Table 1.** CPE data for $Co^{H}$ and $Co^{Me}$ after cronoamperometry over a glassy carbon rod (A = 1.8 $cm^2$) at 1.0 mM [Cat.] in $TBAPF_6$/MeCN 0.1 M electrolyte.

| Cat. | E(V) | $[H_2O]$ (%) | t (min) | Q (C) | $FY_{CO}$ (%) | $TON_{CO}$ |
|---|---|---|---|---|---|---|
| $Co^{H}$ | −1.9 | 10 | 180 | 2.5 | 37 | 1.6 |
| | −1.9[a] | 10 | 60 | 3.4 | 38 | 2.2 |
| | −1.9[b] | 10 | 60 | 2.4 | 96 | 4.0 |
| | −1.9[b] | 10 | 180 | 8.0 | 81 | 11.2 |
| | −2.2 | 1.0 | 60 | 1.7 | 19 | 0.5 |
| $Co^{Me}$ | −2.2 | 1.0 | 60 | 1.5 | 9 | 0.2 |

[a] Temperature control at 30 °C. [b] Experiment under light irradiation (LED, 447 nm, 35 W).

indicate further side reactivity after the C–O bond cleavage step at low potentials. Interestingly, CPE of $Co^{H}$ with a 10% (v/v) of $H_2O$ at the peak potential of the first reduction (−1.9 V vs. $Fc^{+/0}$, Figure 7) produced 1.6 TON of CO with a 37% faradaic yield for CO production ($FY_{CO}$) after 3 h of CPE. These results are in agreement with the three-fold increase in current observed in the CV of $Co^{H}$ with a 10% (v/v) of $H_2O$ and it is also related to the growth of the $[Co^{I}–CO]^+$ and $HCO_3^-/CO_3^{2-}$ signals under IR-SEC conditions at redox potentials close to the $Co^{II/I}$ process.

### 2.5. Mechanistic Discussion

The comparative study presented here indicates that coordinating N–H groups in a pentacoordinate pyridylamino Co complex favour the catalytic reduction of $CO_2$ at the $Co^{II/I}$ reduction (Figure 9). Previous studies have shown that the $CO_2$ binding step can occur over a $Co^{I}$ intermediate in a cyclam-like macrocyclic complex.[23] However, in that example, the catalytic $CO_2$ reduction occurs at more negative potentials. Besides, the sub-stoichiometric formation of $[Co^{I}–CO]^+$ at the $Co^{II/I}$ reduction was observed for tetracoordinate Co complexes with *cis*-labile coordination sites.[10] Although the C–O bond cleavage step was feasible, the concomitant formation of inactive $Co^{II}$-carbonate species prevented the catalytic $CO_2$ reduction at the $Co^{II/I}$ reduction.

The $Co^{H}$ complex presented herein shows catalytic $CO_2$ reduction at the $Co^{II/I}$ redox potential, as observed by CV and CPE at high concentrations of water but also under FTIR-SEC conditions in anhydrous acetonitrile. $Co^{H}$ can boost the $CO_2$ binding step, due to the strong σ-donating character of the coordinating N–H group which increases the nucleophilic character of the Co centre. This inductive electronic effect was also evidenced by the low-energy shift of the $\nu_{st}$(CO) band of the $[Co^{I}–CO]^+$ intermediate caused by the strong π-backbonding (Figure 9). However, we cannot discard the hydrogen bonding by the highly polar N–H group near the $CO_2$ binding site. Moreover, we propose that the effect of the carbonate binding during the catalytic $CO_2$ reduction could be minimized in the case of five- *versus* four- coordinate ligand but also by the high concentration of water (10% (v/v)) present in the reaction media under electrolysis conditions. Our CV experiments with $Co^{H}$ suggested that, at low $H_2O$ concentration, the $CO_2$ reduction rate is proton-dependent. Instead, at high $H_2O$

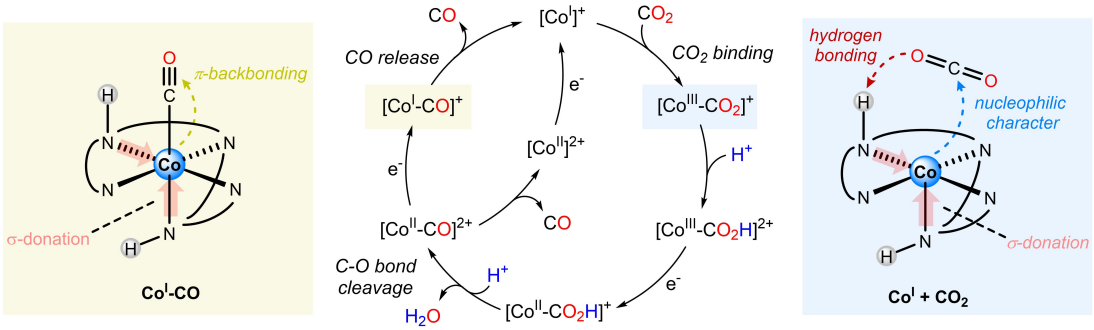


**Figure 9.** Schematic representation of the effect of coordinating N–H groups of **Co$^{H}$** in the $CO_2$ binding step and in the stability of the Co$^{I}$–CO intermediate.

concentration, the peak current does not depend anymore on the concentration of added proton source which is in line with a proton-independent rds at this regime. Thus, in the presence of a 10% (v/v) of water, the catalytic $CO_2$ reduction rate may mainly depend on the CO release and $CO_2$ binding steps (Figure 10). Consequently, for **Co$^{H}$**, the energy barrier mainly depends on the CO release thermodynamics, unlike for **Co$^{Me}$**, whereby the rds involves significantly both the CO release and $CO_2$ binding steps. These data can provide an explanation for the higher current increase observed for **Co$^{H}$** *versus* **Co$^{Me}$** under $CO_2$ reduction conditions at the Co$^{II/I}$ redox potential.

### 2.6. Effect of Light on the Catalytic Performance

Based on earlier reports on CO dissociation from metal carbonyls with light, we proposed that light irradiation can be useful for improving the performance of catalytic systems where the CO release step is involved in the rds of the catalytic cycle.[24] As shown in Figure 11, the pronounced peak shape voltammogram observed in the CV of **Co$^{H}$** indicates a strong catalytic inhibition due to product formation (Figure 11, A).[25] Accordingly to the above reported IR-SEC and DFT data, we attributed such a behaviour to the formation of a highly stable [Co$^{I}$–CO]$^{+}$ intermediate, suggesting that the CO release could be an important bottleneck in the electrocatalytic $CO_2$ reduction. We recently found that an analogous intermediate hinders an efficient $CO_2$ reduction to CO under pure electrochemical conditions by a cobalt catalyst bearing a tetradentate nitrogen ligand at low overpotentials.[10] Therefore, we investigated the effect of light irradiation on the electrocatalytic behaviour of **Co$^{H}$** by using CV and CPE.

Interestingly, when a **Co$^{H}$** solution is irradiated by blue light (447 nm), the current of the catalytic wave of **Co$^{H}$** increases in

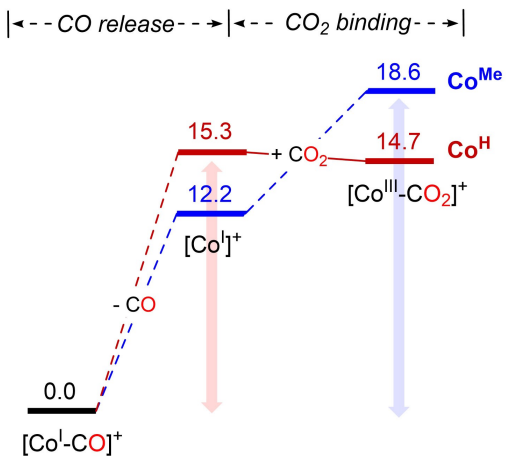


**Figure 10.** Thermodynamic Gibbs energy profile (in kcal·mol$^{-1}$) calculated at the B3LYP-D$_3$/6-31 + G* (SMD, acetonitrile) level of theory of the CO release and $CO_2$ binding steps of the $CO_2$ reduction catalytic cycle with **Co$^{H}$** and **Co$^{Me}$**.

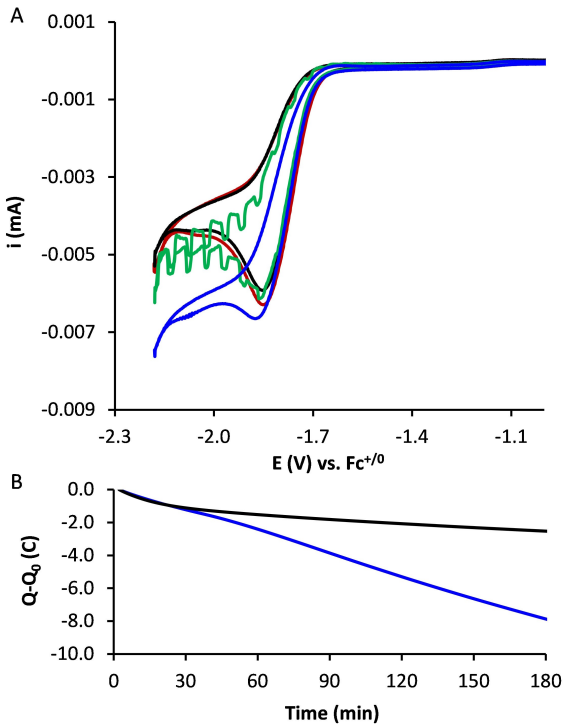


**Figure 11.** A) CV (0.5 V·s$^{-1}$) of **Co$^{H}$** in the dark with temperature control at 22 °C (black), 30 °C (red). CV with chopped light (447 nm, ca. 1 second dark-light cycles, green). CV under 447 nm light irradiation (blue). B) Charge passed in the course of a CPE in the dark at room temperature (black) and under 447 nm light irradiation (blue). Conditions: $CO_2$ atmosphere in TBAPF$_6$/CH$_3$CN (0.1 M) with a 10% of added $H_2O$ over a GC WE disk (ø = 0.1 cm) for CV and rod (A = 1.8 cm$^2$) for CPE.

comparison with the CV recorded in the dark, and the voltammetric shape approaches a canonical S-shaped catalytic voltammogram (Figure 11a, blue curve). These features are consistent with a beneficial effect of light irradiation on catalysis, most likely due to a weaker CO product inhibition due to light-assisted CO release. This was further confirmed by long-term CPE experiments under $CO_2$ with a 10% (v/v) of $H_2O$, which clearly showed a substantial improvement of CO selectivity and catalyst durability under light-assisted CPE. At −1.9 V of applied voltage, **Co$^{H}$** produced 11.2 $TON_{CO}$ with 81% $FY_{CO}$ under light irradiation after 3 hours of CPE, considerably improving the performances in the dark (1.6 TON with a 37% $FY_{CO}$) (Table 1). Notably, light irradiation also increased the catalyst lifetime electrolysis, in contrast with a fast charge decay over time observed during CPE in the dark (Figure 11b).

The effect of temperature was carefully controlled and all the reported electrochemical experiments under light irradiation were carried out under thermostated conditions by using a double-wall jacket glass cell with circulating water. The setup was also fitted with a thermometer to on-line monitoring of the temperature changes in the solution over time. The temperature control was set at 22 °C and only slight heating was observed after a few hours of chronoamperometry, with a maximum recorded temperature of 30 °C. Although it is very challenging to discard any contribution due to local thermal effects on the enhancement observed in the catalytic performances, control experiments suggested that local heating was not the main contributor to the observed changes. Firstly, a temperature-controlled CV at 30 °C in the dark is basically superimposable to the one recorded at 22 °C in the dark, without any evidence of current increase (Figure 11a). On the other hand, when a CV was recorded with chopped light (ca. 1 s light–1 s dark), current was found to increase sharply upon light irradiation and instantaneously decrease in the dark phase (Figure 11a, green curve). Since the temperature changes have larger inertia than light adsorption, these experiments indicate that light is the main responsible of the observed current enhancement in the CV timescale. These results were also confirmed by chronoamperometric data of **Co$^{H}$** at −1.9 V in the dark at 30 °C, which resulted in analogous performances as those observed in the dark experiment at room temperature ($FY_{CO}$ = 38%, 2.2 $TON_{CO}$ after 1 hour, Table 1).

As previously stated, the effect of light in the electrochemical $CO_2$ reduction has been described before for molecular first-row transition metal catalysts.[18b,26] In the case of our previously reported example, the light irradiation effect was observed at the $Co^{I/0}$. Instead, **Co$^{H}$** in the presence of water allows for the quantitative formation of the cobalt-carbonyl intermediate early at the $Co^{II/I}$ redox potential and, therefore, it shows a larger effect of the light-promoted CO release even in the CV timescales. The beneficial effect of light in the catalytic $CO_2$ reduction confirms the strong contribution of the CO release step in the overall kinetics for $CO_2$ reduction, providing a counterbalance to the more donating capacity of the N–H groups in the **Co$^{H}$** complex.

## 3. Conclusions

In this work, it has been investigated the effect of coordinating N–H groups in the electrochemical reduction of $CO_2$ to CO with new molecular Co complexes. With this aim, we have synthesized and characterized **Co$^{H}$** and **Co$^{Me}$**, a new family of pyridylamino $Co^{II}$ complexes based on a new $C_2$-symmetric pentacoordinate chiral ligand. Moreover, we have studied and compared their electrochemical behavior under $CO_2$ reduction conditions by means of CV, FTIR-SEC and CPE. The CV experiments indicate that the $Co^{II/I}$ reduction process of complex **Co$^{H}$** is 200 mV more negative than in **Co$^{Me}$** which implies a stronger nucleophilic character of the $Co^{I}$ intermediate of **Co$^{H}$**. This electronic effect together with the hydrogen bonding ability of the coordinating N–H groups can favor the $CO_2$ binding step to **Co$^{H}$** compared to **Co$^{Me}$**. On the other hand, FTIR-SEC of complexes **Co$^{H}$** and **Co$^{Me}$**, together with the DFT modelling of the IR spectra, revealed the formation of a new $[Co^{I}–CO]^{+}$ resting state intermediate with $\nu_{st}$(CO) bands at 1909 $cm^{-1}$ (**Co$^{Me}$**) and 1896 $cm^{-1}$ (**Co$^{H}$**). The accumulation of such intermediate implies that the C–O bond cleavage can occur relatively fast at the $Co^{II/I}$ redox potential. Moreover, CV in the presence of a 10% (v/v) of water revealed a three-fold increase of current at the $Co^{II/I}$ event which agrees with the clean formation of $[Co^{I}–CO]^{+}$ whereas it was not observed for **Co$^{Me}$**. CPE corroborated that **Co$^{H}$** is catalytically active even at the $Co^{II/I}$ redox wave (−1.9 V vs. $Fc^{+/0}$, 37% $FY_{CO}$, 1.6 $TON_{CO}$). These experimental results, together with the DFT model, suggests that the C–O bond cleavage step can occur relatively fast at the $Co^{II/I}$ wave. Therefore, the CO release is a main bottleneck in the $CO_2$ reduction reaction catalyzed by pyridylamino Co complexes. This results postulate the use of light irradiation as an effective strategy to mitigate the product inhibition in the electrocatalytic $CO_2$ reduction to CO with **Co$^{H}$** (−1.9 V, 81% $FY_{CO}$, 11.2 $TON_{CO}$).

## Experimental Section

### General Methods and Materials

All the procedures were carried out under inert conditions using standard glovebox and Schlenk techniques. The quality of the used gases ($N_2$, Ar and $CO_2$) was 99.9995%. Unless otherwise indicated, solvents and other reagents were purchased from commercial sources and used as received. Anhydrous acetonitrile (Sigma-Aldrich, 99.8%, < 0.001% water) and tetrabutylammonium hexafluorophosphate ($TBAPF_6$, Aldrich, ≥ 99.0%) stored in a glovebox were used in electrochemistry experiments. NMR spectra were recorded on Bruker AV400, AV500 and AVIII500 spectrometers at 298 K with $^{1}H$ chemical shifts (ppm) internally calibrated to the residual protons of the deuterated solvent. All mass spectra were recorded on a MicroTOF Focus II (Bruker Daltonics). Samples were introduced in acetonitrile solution into the mass spectrometer ion source (ESI) by direct injection using a syringe pump. Single crystal X-ray diffraction analysis was performed in an Apex DUO Kappa 4-axis goniometer equipped with an APPEX 2 4 K CCD area detector, a Microfocus Source E025 IuS using $MoK_\alpha$ radiation, Quazar MX multilayer Optics as monochromator and an Oxford Cryosystems low temperature device Cryostream 700 plus ($T$ = −173 °C). Synthe-

ses of ligands $\mathbf{L^H}$ and $\mathbf{L^{Me}}$ and ligand precursors have been based or adapted from reported procedures in the literature.[14] Detailed synthetic procedures and characterization data can be found in section 1 of the SI.

### Synthesis of Co Complexes

In a glovebox, a solution of $Co(OTf)_2(MeCN)_2$ in anhydrous THF was added dropwise to a vigorously stirred solution of the corresponding ligand in THF. Few minutes later, a pale pink precipitate appeared. After stirring for an additional 5 hours the solution was filtered off and the resulting solid dried under vacuum. This solid was dissolved in $CH_2Cl_2$, filtered over Celite® and crystallized by slow diffusion of diethyl ether into this solution producing crystals suitable for X-ray diffraction. A more detailed description for the synthetic procedure of $\mathbf{Co^H}$ and $\mathbf{Co^{Me}}$ and characterization can be found in the SI (section 2).

### Electrochemistry

All the electrochemical experiments were performed with a Bio-Logic VSP or PS-50 potentiostat equipped with the EC-Lab software. For Cyclic Voltammetry (CV) measurements, we have used a single-compartment cell filled with a solution of the complex under study in $TBAPF_6$/CH3CN (0.1 M) electrolyte sparged with Ar or $CO_2$. Glassy carbon disk of 3 mm or 1 mm diameter were used as working electrode (WE), a Pt wire as counter electrode (CE) and a Ag wire inside a bridge tube containing the same electrolyte solution and separated from the working solution by a porous tip as pseudoreference. All redox potentials have been calibrated using ferrocene (Fc) as an internal standard and all the potentials are referenced *versus* $Fc^{+/0}$. For Controlled-Potential Electrolysis (CPE) experiments, we have used a divided cell. The cathodic compartment was filled with a 1 mM solution of the catalyst under study in 3 ml of $TBAPF_6$/$CH_3CN$ (0.1 M) which was constantly stirred in the course of the experiment. A glassy carbon rod (1.8 $cm^2$ surface) was used as a WE together with the same pseudoreference as in the CV experiments. The redox potential of the $Fc^{+/0}$ couple was checked in a separate cell before and after electrolysis. The anodic chamber contained the same electrolyte, and a Pt was used as CE and the two compartments were separated by a ceramic frit.

### Spectroelectrochemistry

An optically transparent thin-layer electrode (OTTLE) cell, equipped with a Pt minigrid WE and CE, an Ag microwire pseudo-reference electrode and a $CaF_2$ window was filled with a $CO_2$-saturated solution of the catalyst under investigation (6 mM) in $TBAPF_6$/$CH_3CN$ (0.2 M). Blank solutions with only electrolyte were used for solvent subtractions. FTIR spectra were recorded on a Nicolet iS50 FT-IR spectrometer equipped with a MCT detector.

### Experiments under Light Irradiation

All electrochemistry experiments under irradiation have been performed with a Luxeon 16 LED lamp (447 nm) connected to a power source at (0.8 A). Under irradiation conditions, the temperature of the cell was controlled with a double jacket cell connected to a cooler set at 20 °C to avoid a temperature increase of more than 10 °C in the solution. Control experiments in the dark were carried out in the same sistem at 30 °C. The temperature inside the cell was corroborated under operation with a thermometer inside the cell in contact with our solution. See section 5 of the SI for a picture of the setup (Figure S21).

### Gas Chromatography and Quantification of Gases

Static analysis of the headspace in photocatalysis was performed by manual injection in an Agilent Technologies 6890 N GC System equipped with a HP-Molsieve column (19095P-MS5) and a Thermal Conductivity Detector (TCD). The quantification of the CO obtained was measured through the interpolation of a previous calibration known dilutions of syngas in $CO_2$.

### DFT Calculations

All calculations have been performed in Gaussian09 software package. The geometry optimization and vibrational frequency analysis of the different intermediates have been performed at the B3LYP-$D_3$/6-31 + G*(SMD, acetonitrile) level of theory. All computationally obtained vibrational frequency values given in the main text have been corrected by a scaling factor of 0.967 as previously described for the B3LYP/6-31 + G* methodology.[27] The Chemcraft software has been employed for the visualization of the structures. A table with energies and the xyz coordinates of optimized geometries can be found in the SI (section 6.2).

## Acknowledgements

*The authors acknowledge the financial support of the ICIQ Foundation, the CERCA Program/Generalitat de Catalunya, MICINN through Severo Ochoa Excellence Accreditation 2020–2023 (CEX2019-000925-S, MIC/AEI), the European Research Foundation for H2020 project ERC-2015-CoG GREENLIGHT_REDCAT 648304, (J.L.-F.), the Spanish Ministry of Universities for an FPU fellowship FPU16/04234 (S.F.), MINECO for a Severo Ochoa FPI fellowship BES-2015-072152 (S.C.), AGAUR 2017-SGR-1647 (J.L.-F.) and 2017SGR39 (J.M.L.), MINECO/FEDER grant PID2019-109236RB-I00 (M.A.P.), and MICINN (PID2019-110050RB-I00, J.L–F.; PGC2018-098212-B-C22, J.M.L).*

## Conflict of Interest

The authors declare no conflict of interest.

**Keywords:** $CO_2$ reduction · reaction mechanisms · electrocatalysis · cyclic voltammetry · spectroelectrochemistry

[1] P. De Luna, C. Hahn, D. Higgins, S. A. Jaffer, T. F. Jaramillo, E. H. Sargent, *Science* **2019**, *364*, eaav3506.
[2] O. S. Bushuyev, P. De Luna, C. T. Dinh, L. Tao, G. Saur, J. van de Lagemaat, S. O. Kelley, E. H. Sargent, *Joule* **2018**, *2*, 825–832.
[3] F. Franco, S. Fernández, J. Lloret-Fillol, *Curr. Opin. Electrochem.* **2019**, *15*, 109–117.
[4] F. Franco, C. Rettenmaier, H. S. Jeon, B. Roldan Cuenya, *Chem. Soc. Rev.* **2020**, *49*, 6884–6946.
[5] E. Boutin, M. Robert, *Trends in Chemistry* **2021**, *3*, 359–372.
[6] a) S. Fukuzumi, Y.-M. Lee, H. S. Ahn, W. Nam, *Chem. Sci.* **2018**, *9*, 6017–6034; b) E. Boutin, L. Merakeb, B. Ma, B. Boudy, M. Wang, J. Bonin, E. Anxolabéhère-Mallart, M. Robert, *Chem. Soc. Rev.* **2020**, *49*, 5772–5809.
[7] a) K. E. Dalle, J. Warnan, J. J. Leung, B. Reuillard, I. S. Karmel, E. Reisner, *Chem. Rev.* **2019**, *119*, 2752–2875; b) M. Wang, K. Torbensen, D. Salvatore, S. Ren, D. Joulié, F. Dumoulin, D. Mendoza, B. Lassalle-Kaiser, U. Işci, C. P. Berlinguette, M. Robert, *Nat. Commun.* **2019**, *10*, 3602; c) S.

Ren, D. Joulié, D. Salvatore, K. Torbensen, M. Wang, M. Robert, C. P. Berlinguette, *Science* **2019**, *365*, 367–369; d) S. Lin, C. S. Diercks, Y.-B. Zhang, N. Kornienko, E. M. Nichols, Y. Zhao, A. R. Paris, D. Kim, P. Yang, O. M. Yaghi, C. J. Chang, *Science* **2015**, *349*, 1208; e) G. C. Dubed Bandomo, S. S. Mondal, F. Franco, A. Bucci, V. Martin-Diaconescu, M. A. Ortuño, P. H. van Langevelde, A. Shafir, N. López, J. Lloret-Fillol, *ACS Catal.* **2021**, *11*, 7210–7222.

[8] J. Schneider, H. Jia, J. T. Muckerman, E. Fujita, *Chem. Soc. Rev.* **2012**, *41*, 2036–2051.

[9] a) C. Costentin, S. Drouet, G. Passard, M. Robert, J.-M. Savéant, *J. Am. Chem. Soc.* **2013**, *135*, 9023–9031; b) C. Costentin, M. Robert, J.-M. Savéant, *Acc. Chem. Res.* **2015**, *48*, 2996–3006; c) J. Bonin, A. Maurin, M. Robert, *Coord. Chem. Rev.* **2017**, *334*, 184–198; d) J.-M. Savéant, *Chem. Rev.* **2008**, *108*, 2348–2378; e) J. A. Keith, K. A. Grice, C. P. Kubiak, E. A. Carter, *J. Am. Chem. Soc.* **2013**, *135*, 15823–15829; f) X. Su, K. M. McCardle, L. Chen, J. A. Panetier, J. W. Jurss, *ACS Catal.* **2019**, *9*, 7398–7408; g) S. Dey, M. E. Ahmed, A. Dey, *Inorg. Chem.* **2018**, *57*, 5939–5947; h) K. T. Ngo, M. McKinnon, B. Mahanti, R. Narayanan, D. C. Grills, M. Z. Ertem, J. Rochford, *J. Am. Chem. Soc.* **2017**, *139*, 2604–2618; i) D. C. Grills, M. Z. Ertem, M. McKinnon, K. T. Ngo, J. Rochford, *Coord. Chem. Rev.* **2018**, *374*, 173–217.

[10] S. Fernández, F. Franco, C. Casadevall, V. Martin-Diaconescu, J. M. Luis, J. Lloret-Fillol, *J. Am. Chem. Soc.* **2020**, *142*, 120–133.

[11] a) M. Beley, J. P. Collin, R. Ruppert, J. P. Sauvage, *J. Am. Chem. Soc.* **1986**, *108*, 7461–7467; b) E. Fujita, C. Creutz, N. Sutin, D. J. Szalda, *J. Am. Chem. Soc.* **1991**, *113*, 343–353; c) F. Franco, C. Cometto, F. Ferrero Vallana, F. Sordello, E. Priola, C. Minero, C. Nervi, R. Gobetto, *Chem. Commun.* **2014**, *50*, 14670–14673; d) C. Costentin, S. Drouet, M. Robert, J.-M. Savéant, *Science* **2012**, *338*, 90; e) A. Rosas-Hernández, H. Junge, M. Beller, M. Roemelt, R. Francke, *Catal. Sci. Technol.* **2017**, *7*, 459–465; f) A. Chapovetsky, M. Welborn, J. M. Luna, R. Haiges, T. F. Miller, S. C. Marinescu, *ACS Cent. Sci.* **2018**, *4*, 397–404.

[12] a) J. D. Froehlich, C. P. Kubiak, *J. Am. Chem. Soc.* **2015**, *137*, 3565–3573; b) S. Gonell, M. D. Massey, I. P. Moseley, C. K. Schauer, J. T. Muckerman, A. J. M. Miller, *J. Am. Chem. Soc.* **2019**, *141*, 6658–6671; c) S. Gonell, E. A. Assaf, K. D. Duffee, C. K. Schauer, A. J. M. Miller, *J. Am. Chem. Soc.* **2020**, *142*, 8980–8999; d) S. Gonell, J. Lloret-Fillol, A. J. M. Miller, *ACS Catal.* **2021**, *11*, 615–626.

[13] N. C. Maity, P. Kumar Bera, D. Ghosh, S. H. R. Abdi, R. I. Kureshy, N.-u. H Khan, H. C. Bajaj, E. Suresh, *Catal. Sci. Technol.* **2014**, *4*, 208–217.

[14] S. Cañellas, P. Alonso, M. À Pericàs, *Org. Lett.* **2018**, *20*, 4806–4810.

[15] a) A. Call, C. Casadevall, F. Acuña-Parés, A. Casitas, J. Lloret-Fillol, *Chem. Sci.* **2017**, *8*, 4739–4749; b) A. Call, F. Franco, N. Kandoth, S. Fernández, M. González-Béjar, J. Pérez-Prieto, J. M. Luis, J. Lloret-Fillol, *Chem. Sci.* **2018**, *9*, 2609–2619.

[16] a) A. Call, Z. Codolà, F. Acuña-Parés, J. Lloret-Fillol, *Chem. Eur. J.* **2014**, *20*, 6171–6183; b) A. Call, C. Casadevall, A. Romero-Rivera, V. Martin-Diaconescu, D. J. Sommer, S. Osuna, G. Ghirlanda, J. Lloret-Fillol, *ACS Catal.* **2019**, *9*, 5837–5846.

[17] J. D. Froehlich, C. P. Kubiak, *Inorg. Chem.* **2012**, *51*, 3932–3934.

[18] a) J. M. Savéant, C. Costentin, *Elements of Molecular and Biomolecular Electrochemistry: An Electrochemical Approach to Electron Transfer Chemistry*, Wiley, **2019**; b) C. Cometto, L. Chen, P.-K. Lo, Z. Guo, K.-C. Lau, E. Anxolabéhère-Mallart, C. Fave, T.-C. Lau, M. Robert, *ACS Catal.* **2018**, *8*, 3411–3417; c) C. Costentin, M. Robert, J.-M. Savéant, *Chem. Soc. Rev.* **2013**, *42*, 2423–2436.

[19] a) D. W. Shaffer, S. I. Johnson, A. L. Rheingold, J. W. Ziller, W. A. Goddard, R. J. Nielsen, J. Y. Yang, *Inorg. Chem.* **2014**, *53*, 13031–13041; b) D. J. Szalda, E. Fujita, C. Creutz, *Inorg. Chem.* **1989**, *28*, 1446–1450; c) J.-W. Wang, K. Yamauchi, H.-H. Huang, J.-K. Sun, Z.-M. Luo, D.-C. Zhong, T.-B. Lu, K. Sakai, *Angew. Chem. Int. Ed.* **2019**, *58*, 10923–10927; *Angew. Chem.* **2019**, *131*, 11039–11043.

[20] F. Franco, C. Cometto, L. Nencini, C. Barolo, F. Sordello, C. Minero, J. Fiedler, M. Robert, R. Gobetto, C. Nervi, *Chem. Eur. J.* **2017**, *23*, 4782–4793.

[21] G. Fachinetti, G. Fochi, T. Funaioli, *J. Organomet. Chem.* **1986**, *301*, 91–97.

[22] L. E. Lieske, A. L. Rheingold, C. W. Machan, *Sustain. Energy Fuels* **2018**, *2*, 1269–1277.

[23] D. A. Gangi, R. R. Durand, *J. Chem. Soc. Chem. Commun.* **1986**, 697–699.

[24] a) M. Wrighton, *Chem. Rev.* **1974**, *74*, 401–430; b) M. F. Mirbach, M. J. Mirbach, R. W. Wegman, *Organometallics* **1984**, *3*, 900–903.

[25] C. Costentin, S. Drouet, M. Robert, J.-M. Savéant, *J. Am. Chem. Soc.* **2012**, *134*, 11235–11242.

[26] A. Fukatsu, M. Kondo, Y. Okabe, S. Masaoka, *J. Photochem. Photobiol. A* **2015**, *313*, 143–148.

[27] M. Kieninger, O. N. Ventura, *Int. J. Quantum Chem.* **2011**, *111*, 1843–1857.

Manuscript received: June 23, 2021
Revised manuscript received: August 11, 2021
Accepted manuscript online: August 25, 2021